Commun. Comput. Phys.
doi: 10.4208/cicp.150311.090112a

Vol. **12**, No. 5, pp. 1307-1328
November 2012

A Conservative Lagrangian Scheme for Solving Compressible Fluid Flows with Multiple Internal Energy Equations

Juan Cheng[1,*], Chi-Wang Shu[2] and Qinghong Zeng[3]

[1] *National Key Laboratory of Science and Technology on Computational Physics, Institute of Applied Physics and Computational Mathematics, Beijing 100088, China.*
[2] *Division of Applied Mathematics, Brown University, Providence, RI 02912, USA.*
[3] *Institute of Applied Physics and Computational Mathematics, Beijing 100088, China.*

Received 15 March 2011; Accepted (in revised version) 9 January 2012

Available online 8 May 2012

Abstract. Lagrangian methods are widely used in many fields for multi-material compressible flow simulations such as in astrophysics and inertial confinement fusion (ICF), due to their distinguished advantage in capturing material interfaces automatically. In some of these applications, multiple internal energy equations such as those for electron, ion and radiation are involved. In the past decades, several staggered-grid based Lagrangian schemes have been developed which are designed to solve the internal energy equation directly. These schemes can be easily extended to solve problems with multiple internal energy equations. However such schemes are typically not conservative for the total energy. Recently, significant progress has been made in developing cell-centered Lagrangian schemes which have several good properties such as conservation for all the conserved variables and easiness for remapping. However, these schemes are commonly designed to solve the Euler equations in the form of the total energy, therefore they cannot be directly applied to the solution of either the single internal energy equation or the multiple internal energy equations without significant modifications. Such modifications, if not designed carefully, may lead to the loss of some of the nice properties of the original schemes such as conservation of the total energy. In this paper, we establish an equivalency relationship between the cell-centered discretizations of the Euler equations in the forms of the total energy and of the internal energy. By a carefully designed modification in the implementation, the cell-centered Lagrangian scheme can be used to solve the compressible fluid flow with one or multiple internal energy equations and meanwhile it does not lose its total energy conservation property. An advantage of this approach is that it can be easily applied to many existing large application codes which are based on the framework of solving multiple internal energy equations. Several two dimensional numerical examples for both Euler equations and three-temperature hydrodynamic equations in

*Corresponding author. *Email addresses:* cheng_juan@iapcm.ac.cn (J. Cheng), shu@dam.brown.edu (C.-W. Shu), zeng_qinghong@iapcm.ac.cn (Q. Zeng)

 ©2012 Global-Science Press

cylindrical coordinates are presented to demonstrate the performance of the scheme in terms of symmetry preserving, accuracy and non-oscillatory performance.

AMS subject classifications: 65M06, 76M20

Key words: Lagrangian scheme, conservative, cell-centered, internal energy equation, compressible fluid flow, three-temperature model.

1 Introduction

The Lagrangian methods, in which the mesh moves with the local fluid velocity, are widely used in many fields for multi-material flow simulations such as in astrophysics and inertial confinement fusion (ICF), due to their distinguished advantage in capturing material interfaces automatically. Such methods can be classified into two types, one is the staggered-grid based Lagrangian method, the other is the cell-centered Lagrangian method. For the staggered-grid based Lagrangian method, the algorithms are built on a staggered discretization in which velocity (momentum) is stored at vertices, while density and internal energy are stored at cell centers. The density/internal energy and velocity are solved on two different control volumes directly, see, e.g., [1, 3, 4, 6, 25, 29]. An artificial viscosity term [5, 7, 29] is usually added to the scheme to prevent spurious oscillations near the discontinuities. As the internal energy equation is discretized directly, this kind of methods usually cannot keep the conservation of the total energy, unless a specially designed compatible construction is used, see [6]. On the other hand, for the cell-centered Lagrangian schemes, density, momentum and total energy are all stored at the cell center and evolved on the same control volume directly. This kind of methods has several advantages such as easiness for remapping when necessary, no need for explicit artificial viscosity for shock capturing and conservation for all the conserved variables including mass, momentum and total energy. In recent years, the cell-centered Lagrangian method has been developed rapidly and many cell-centered schemes have been presented [8, 10–12, 14, 19–24, 26, 28] and they are demonstrated to have good properties such as conservation, accuracy and non-oscillation.

In some hydrodynamic application problems in, e.g., ICF and astrophysics, multiple internal energy equations are involved. For example, the 2D code CHIC [2] applied to simulate the ICF problem involves electron and ion internal energy equations and it is based on a cell-centered Lagrangian scheme discretizing the electron internal energy equation and total energy equation directly. However, most of the existing large codes used in these fields are originally based on the staggered-grid Lagrangian schemes and are designed to solve the internal energy equations directly, e.g., the LASNEX [17], HYDRA [27] and LARED-H [30] codes. As the cell-centered Lagrangian schemes are commonly discretized from the Euler equations in the form of the total energy, it is difficult to use them in these codes without significant modifications. If such modifications are not

designed carefully, some of the original good properties such as the conservation of the total energy may be lost.

In this paper, we establish an equivalency relationship between the cell-centered Lagrangian discretizations of the Euler equations in the forms of the total energy and of the internal energy. By a suitable modification in the implementation, the cell-centered Lagrangian scheme can be used to solve Euler equations with internal energy without the loss of its good properties such as the conservation of total energy. In fact, the schemes for the Euler equations in the forms of the total energy and of the internal energy are equivalent mathematically. The main advantage of this new strategy of implementation is that the scheme can then be directly extended to solve the compressible flow with multiple internal energy equations, which is carried out in this paper. The extended scheme can keep its original good properties such as the conservation of the total energy and spherical symmetry easily. This also allows the cell-centered schemes to be conveniently applied to existing large application codes which involve multiple internal energy equations and are originally based on staggered-grid schemes, for example the LARED-H radiation hydrodynamic code [30].

An outline of the rest of this paper is as follows. In Section 2, we establish the relationship between the discretizations of the Euler equations in the forms of the total energy and of the internal energy. Several numerical examples for Euler equations are given to demonstrate the performance of the above mentioned technique. In Section 3, we discuss the discretization of the three-temperature radiation hydrodynamic equations and show the numerical result obtained by the LARED-H code with the cell-centered Lagrangian scheme. In Section 4 we will give concluding remarks.

2 Solving the compressible Euler equations in the form of the internal energy by conservative Lagrangian schemes

2.1 The establishment of an equivalency relationship between the Lagrangian discretizations of the compressible Euler equations in the forms of the total energy and of the internal energy

We consider the compressible inviscid flow governed by the Euler equations which have the following integral form in the Lagrangian formulation

$$\frac{d}{dt}\iint_{\Omega(t)}\rho dV=0, \tag{2.1a}$$

$$\frac{d}{dt}\iint_{\Omega(t)}\rho\mathbf{u}dV=-\int_{\Gamma(t)}P\mathbf{n}ds, \tag{2.1b}$$

$$\frac{d}{dt}\iint_{\Omega(t)}EdV=-\int_{\Gamma(t)}Pu_nds, \tag{2.1c}$$

where ρ is the density, P is the pressure, E is the total energy, $\mathbf{u}$ is the velocity vector and $\mathbf{M}=\rho\mathbf{u}$ is the momentum.

The set of equations is completed by the addition of an equation of state (EOS) with the following general form

$$P=P(\rho,e), \tag{2.2}$$

where $e=E-\rho\mathbf{u}^2/2$ is the internal energy. Especially, if we consider the ideal gas, then the equation of state has a simpler form

$$P=(\gamma-1)e,$$

where γ is a constant representing the ratio of specific heat capacities of the fluid.

The energy equation in the Euler equations can also be described in the following internal energy form

$$\frac{d}{dt}\iint_{\Omega(t)} edV=-\iint_{\Omega(t)} P\nabla\cdot\mathbf{u}dV. \tag{2.3}$$

Eq. (2.1c) and Eq. (2.3) are mathematically equivalent, however schemes based on them are usually quite different. Conservative schemes are naturally obtained from the Euler equations in the conservative form (2.1a)-(2.1c) which can keep the conservation of mass, momentum and total energy. On the other hand, schemes based on the Euler equations in the nonconservative form (2.1a), (2.1b) and (2.3) are difficult to preserve the conservation of the total energy.

In this section, we establish an equivalency relationship between the Lagrangian discretizations of the compressible Euler equations in the forms of the total energy and of the internal energy. By this technique, we can solve the Euler equations in the form of the internal energy and the more complicated compressible fluid flow with multiple internal energy equations by the conservative Lagrangian schemes easily.

Suppose the 2D spatial domain Ω is discretized into quadralateral computational cells, each quadrangular cell Ω_c being assigned a unique index c. The boundary of the cell Ω_c is denoted as $\partial\Omega_c$. We denote,

$$\begin{aligned}
&m_c=\iint_{\Omega_c}\rho dV,\\
&\overline{\rho}_c=\frac{1}{V_c}\iint_{\Omega_c}\rho dV, \qquad && \overline{\mathbf{M}}_c=\frac{1}{V_c}\iint_{\Omega_c}\mathbf{M}dV,\\
&\overline{E}_c=\frac{1}{V_c}\iint_{\Omega_c}EdV, && \overline{\mathbf{u}}_c=\frac{\overline{\mathbf{M}}_c}{\overline{\rho}_c},
\end{aligned}$$

where V_c and m_c are the volume and mass of the cell Ω_c respectively and $\overline{\mathbf{M}}_c$ and $\overline{E}_c$ are the cell averages of the momentum and the total energy in the cell Ω_c respectively. $\overline{\mathbf{u}}_c$, as the ratio of the cell averages of the momentum and density, is equal to the point value of the velocity at the cell centroid or its cell average up to second order accuracy. For the Lagrangian scheme, the cell mass m_c does not change during the time evolution. The internal energy $\overline{e}_c$ is *defined* as follows,

$$\overline{e}_c=\overline{E}_c-\frac{1}{2}\overline{\rho}_c\overline{\mathbf{u}}_c^2, \tag{2.4}$$

which is equal to the point value of the internal energy at the cell centroid or its cell average up to second order accuracy. Notice that the equality (2.4) is used only in the theoretical derivation below to establish the equivalency of the Lagrangian scheme in the forms of the total energy and of the internal energy. In the actual implementation of the scheme, its influence is limited to the initial condition for the internal energy only. Even for the initial condition, we are not required to take the internal energy based on (2.4), but are free to choose it in any other way within the accuracy of the scheme, for example by the point values or cell averages of the initial internal energy for up to second order schemes. Without loss of generality, we write the first-order conservative cell-centered Lagrangian scheme for the equations of momentum and total energy (2.1b)-(2.1c) in the following form,

$$\overline{\mathbf{M}}_c^{n+1}V_c^{n+1}-\overline{\mathbf{M}}_c^{n}V_c^{n}=\Delta t\mathbf{F}_M, \tag{2.5a}$$

$$\overline{E}_c^{n+1}V_c^{n+1}-\overline{E}_c^{n}V_c^{n}=\Delta tF_E, \tag{2.5b}$$

where $\mathbf{F}_M$ and F_E represent the spacial discretization operators approximating the right-hand-side terms of Eqs. (2.1b)-(2.1c) respectively. Both $\mathbf{F}_M$ and F_E are determined by the values of the numerical solution at the n-th time step, while different schemes give different expressions of these terms, see, e.g., [12, 13, 20, 24] for several possible choices. The superscripts n, $n+1$ represent the variables at the n-th and $(n+1)$-th time steps respectively.

The scheme to solve the internal energy equation (2.3) is expressed as follows,

$$\overline{e}_c^{n+1}V_c^{n+1}-\overline{e}_c^{n}V_c^{n}=\Delta tF_e, \tag{2.6}$$

where F_e stands for the spacial discretization operator approximating the right-hand-side term of Eq. (2.3). In summary, we have

$$\mathbf{F}_M\simeq-\int_{\partial\Omega_c}P\mathbf{n}ds,\qquad F_E\simeq-\int_{\partial\Omega_c}Pu_nds,\qquad F_e\simeq-\iint_{\Omega_c}P\nabla\cdot\mathbf{u}dV. \tag{2.7}$$

Next, we would like to establish an equivalency relationship between (2.5b) and (2.6), that is, we attempt to determine F_e by the expressions (2.5a)-(2.5b).

Subtracting (2.5a) multiplied by $(\overline{\mathbf{u}}_c^{n+1}+\overline{\mathbf{u}}_c^{n})/2$ from (2.5b) and using the fact that $m_c=\overline{\rho}_c^{n+1}V_c^{n+1}=\overline{\rho}_c^{n}V_c^{n}$, we get

$$\left[\overline{E}_c^{n+1}-\frac{1}{2}\overline{\rho}_c^{n+1}(\overline{\mathbf{u}}_c^{n+1})^2\right]V_c^{n+1}-\left[\overline{E}_c^{n}-\frac{1}{2}\overline{\rho}_c^{n}(\overline{\mathbf{u}}_c^{n})^2\right]V_c^{n}=\Delta t\left[F_E-\frac{1}{2}(\overline{\mathbf{u}}_c^{n+1}+\overline{\mathbf{u}}_c^{n})\cdot\mathbf{F}_M\right]. \tag{2.8}$$

Due to (2.4), we have

$$\overline{e}_c^{n+1}V_c^{n+1}-\overline{e}_c^{n}V_c^{n}=\Delta t\left[F_E-\frac{1}{2}(\overline{\mathbf{u}}_c^{n+1}+\overline{\mathbf{u}}_c^{n})\cdot\mathbf{F}_M\right]. \tag{2.9}$$

Thus, we can choose F_e as follows,

$$F_e=F_E-\frac{1}{2}(\overline{\mathbf{u}}_c^{n+1}+\overline{\mathbf{u}}_c^{n})\cdot\mathbf{F}_M. \tag{2.10}$$

Remark 2.1. The scheme (2.6) with F_e given by (2.10) is an explicit scheme even if it looks like an implicit scheme due to the appearance of $\overline{\mathbf{u}}_c^{n+1}$. This is because, at each time step, we can solve the momentum equation (2.5a) first and get $\overline{\mathbf{u}}_c^{n+1}$ before the scheme (2.6) is evolved.

Remark 2.2. The discretization (2.5a), (2.6) with F_e given by (2.10) is not a new scheme. It is just a mathematically equivalent implementation of the discretization (2.5a)-(2.5b), hence it enjoys the same properties such as the conservation for momentum and total energy. The difference in these two discretizations is purely in their implementation. By this modification in the implementation, the cell-centered Lagrangian scheme can be used to solve the Euler equations in the form of the internal energy directly and it also can be easily extended to solve the compressible fluid flow with multiple internal energy equations, which will be described in the next section.

Remark 2.3. The relationship (2.10) holds for any first-order cell-centered Lagrangian scheme in any coordinate system such as the cartesian, cylindrical or spherical coordinates which can be written in the form (2.5a)-(2.6). This technique can also be extended to second order accurate schemes with the TVD Runge-Kutta time discretization. Such an extension will however not be discussed in this paper and will be left for future work.

2.2 Numerical tests for Euler equations in two-dimensional cylindrical coordinates

2.2.1 The specific Lagrangian scheme used in the numerical tests

In this subsection, without loss of generality, we choose the cell-centered Lagrangian scheme given in the paper [13], which is a modified version of the cell-centered control volume scheme proposed by Maire in [20], to validate the technique introduced in the previous subsection. This scheme has several good properties such as the conservation of mass, momentum and total energy, compatibility with the geometric conservation law (GCL), robustness and one-dimensional spherical symmetry in a two-dimensional cylindrical geometry when computed on an equal-angle-zoned initial grid.

The governing equations and the scheme are summarized as follows. We solve the Euler equations in the cylindrical coordinates and in the form of the internal energy with the following control volume formulation

$$m_c \frac{\mathrm{d}}{\mathrm{d}t}\Big(\frac{1}{\overline{\rho}_c}\Big) = \int_{\partial\Omega_c} \mathbf{u}\cdot\mathbf{n} r dl, \qquad \frac{\mathrm{d}}{\mathrm{d}t}(\overline{M}_c^z V_c) = -\int_{\partial\Omega_c} P n_z r dl, \tag{2.11a}$$

$$\frac{\mathrm{d}}{\mathrm{d}t}(\overline{M}_c^r V_c) = -\int_{\partial\Omega_c} P n_r r \mathrm{d}l + \iint_{\Omega_c} P dz dr, \qquad \frac{\mathrm{d}}{\mathrm{d}t}(\overline{e}_c V_c) = -\iint_{\Omega_c} P\nabla\cdot\mathbf{u} r dz dr, \tag{2.11b}$$

where z and r are the axial and radial coordinates respectively, $\overline{\mathbf{M}}_c = (\overline{M}_c^z, \overline{M}_c^r)$. The first equation is derived from the mass equation and the geometric conservation law (GCL),

$$\frac{\mathrm{d}}{\mathrm{d}t}\iint_{\Omega_c} dV = \int_{\partial\Omega_c} \mathbf{u}\cdot\mathbf{n} r dl. \tag{2.12}$$

Following the notations used in [20], in this cell-centered control volume Lagrangian scheme, each node of the mesh is assigned a unique index p and we denote the counterclockwise ordered list of the four nodes of the cell Ω_c by $p(c)$. A_c is used to denote the area of the cell Ω_c. The coordinates and velocity of the point p are denoted as (z_p,r_p) and $\mathbf{u}_p=(u_p^z,u_p^r)$ respectively. Two nodal pressures related to the two edges sharing the node p are defined at each node p of the cell Ω_c which are denoted as $\pi_{\underline{p}}^c$ and $\pi_{\overline{p}}^c$, the half lengths and the unit outward normals of the edges connecting the point p are denoted as $l_{\underline{p}}^c,l_{\overline{p}}^c$ and $\mathbf{n}_{\underline{p}}^c,\mathbf{n}_{\overline{p}}^c$ individually, see Fig. 1.

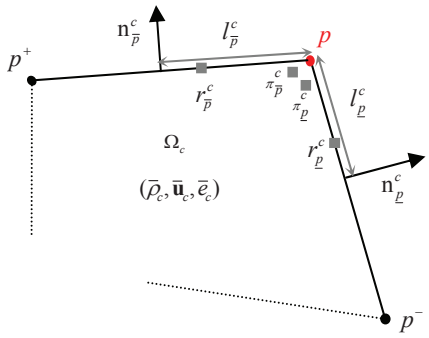

Figure 1: Notations related to the cell Ω_c.

To clarify the determination of the nodal velocity, we further give some notations to describe the cell edges related to the point p. The list of edges passing through the point p is denoted by $E(p)$. For the edge $e\in E(p)$, we denote its other end point as p', which corresponds to p^- or p^+ shown in Fig. 1. Denote its direction to be from p to p' and its length to be l_p^e. $\mathbf{n}_p^e=(n_p^{e,z},n_p^{e,r})$ is its unit outward normal direction. v_p^e is its normal velocity. The variables with the subscripts cl and cr are the values of the corresponding cell-centered variables in its left and right cells respectively.

The specific formula to calculate the nodal velocity used in this paper is as follows [20, 24],

$$A_p\mathbf{u}_p=\mathbf{b}_p, \tag{2.13}$$

where

$$A_p=\begin{pmatrix} a_{11} & a_{12} \\ a_{21} & a_{22} \end{pmatrix}, \qquad \mathbf{b}_p=\sum_{e\in E(p)} r_p^e l_p^e(\rho_{cl}a_{cl}+\rho_{cr}a_{cr})v_p^e\mathbf{n}_p^e, \tag{2.14}$$

with

$$\begin{aligned} a_{11}&=\sum_{e\in E(p)} r_p^e l_p^e(\rho_{cl}a_{cl}+\rho_{cr}a_{cr})(n_p^e)_z^2,\\ a_{22}&=\sum_{e\in E(p)} r_p^e l_p^e(\rho_{cl}a_{cl}+\rho_{cr}a_{cr})(n_p^e)_r^2,\\ a_{12}=a_{21}&=\sum_{e\in E(p)} r_p^e l_p^e(\rho_{cl}a_{cl}+\rho_{cr}a_{cr})(n_p^e)_z(n_p^e)_r. \end{aligned}$$

Also, $r_p^e=(2r_p+r_{p'})/3$ and a_{cl}, a_{cr} are the local speeds of sound in the relevant cells. The edge's normal velocity v_p^e is determined by the following acoustic Riemann solver along the normal direction $\mathbf{n}_p^e$,

$$v_p^e=\frac{(\rho_{cl}a_{cl}\mathbf{u}_{cl}+\rho_{cr}a_{cr}\mathbf{u}_{cr})\cdot\mathbf{n}_p^e-P_{cr}+P_{cl}}{\rho_{cl}a_{cl}+\rho_{cr}a_{cr}}. \tag{2.15}$$

The formulas to calculate the nodal pressures $\pi_{\underline{p}}^c$ and $\pi_{\overline{p}}^c$ are as follows

$$P_c-\pi_{\underline{p}}^c=\rho_c a_c(\mathbf{u}_p-\overline{\mathbf{u}}_c)\cdot\mathbf{n}_{\underline{p}}^c,\qquad P_c-\pi_{\overline{p}}^c=\rho_c a_c(\mathbf{u}_p-\overline{\mathbf{u}}_c)\cdot\mathbf{n}_{\overline{p}}^c, \tag{2.16}$$

where P_c is the pressure of the cell Ω_c determined by $\{\overline{\rho}_c,\overline{\mathbf{u}}_c,\overline{e}_c\}$. $r_{\underline{p}}^c$ and $r_{\overline{p}}^c$ are defined as

$$r_{\underline{p}}^c=\frac{1}{3}(2r_p+r_{p^-}),\qquad r_{\overline{p}}^c=\frac{1}{3}(2r_p+r_{p^+}),$$

where p^-,p^+ are the two neighboring points of the point p (see Fig. 1).

The equation of nodal movement is discretized as

$$z_p^{n+1}=z_p^n+\Delta t^n u_p^{z,n},\qquad r_p^{n+1}=r_p^n+\Delta t^n u_p^{r,n}, \tag{2.17}$$

where $u_p^{z,n},u_p^{r,n}$ are the z and r components of $\mathbf{u}_p$ at the n-th time step. (z_p^n,r_p^n), (z_p^{n+1},r_p^{n+1}) are the z and r coordinates of the point p at the n-th and $(n+1)$-th time steps respectively.

The fully discretized scheme for Eq. (2.11) is written as follows

$$m_c\Big(\frac{1}{\overline{\rho}_c^{n+1}}-\frac{1}{\overline{\rho}_c^n}\Big)=\Delta t^n F_m, \tag{2.18a}$$

$$\overline{M}_c^{z,n+1}V_c^{n+1}-\overline{M}_c^{z,n}V_c^n=\Delta t^n F_M^z,\qquad \overline{M}_c^{r,n+1}V_c^{n+1}-\overline{M}_c^{r,n}V_c^n=\Delta t^n F_M^r, \tag{2.18b}$$

$$\overline{e}_c^{n+1}V_c^{n+1}-\overline{e}_c^nV_c^n=\Delta t^n\Big(F_E-\frac{1}{2}((\overline{u}_c^{z,n+1}+\overline{u}_c^{z,n})F_M^z+(\overline{u}_c^{r,n+1}+\overline{u}_c^{r,n})F_M^r)\Big), \tag{2.18c}$$

where $V_c^{n+1}=m_c/\overline{\rho}_c^{n+1}$, $V_c^n=m_c/\overline{\rho}_c^n$. $\overline{\mathbf{M}}_c^n=(\overline{M}_c^{z,n},\overline{M}_c^{r,n})$, $\overline{\mathbf{M}}_c^{n+1}=(\overline{M}_c^{z,n+1},\overline{M}_c^{r,n+1})$, $\overline{\mathbf{u}}_c^n=(\overline{u}_c^{z,n},\overline{u}_c^{r,n})$ and $\overline{\mathbf{u}}_c^{n+1}=(\overline{u}_c^{z,n+1},\overline{u}_c^{r,n+1})$ are the cell averages of the momentum and velocity in the cell Ω_c at the n-th and $(n+1)$-th steps respectively. Also

$$F_m=\sum_{p\in p(c)}(r_{\underline{p}}^{c,n}l_{\underline{p}}^{c,n}\mathbf{n}_{\underline{p}}^{c,n}+r_{\overline{p}}^{c,n}l_{\overline{p}}^{c,n}\mathbf{n}_{\overline{p}}^{c,n})\cdot\mathbf{u}_p^n, \tag{2.19a}$$

$$F_M^z=-\sum_{p\in p(c)}(r_{\underline{p}}^{c,n}l_{\underline{p}}^{c,n}\pi_{\underline{p}}^{c,n}n_{\underline{p}}^{c,z,n}+r_{\overline{p}}^{c,n}l_{\overline{p}}^{c,n}\pi_{\overline{p}}^{c,n}n_{\overline{p}}^{c,z,n}), \tag{2.19b}$$

$$F_M^r=-\sum_{p\in p(c)}(r_{\underline{p}}^{c,n}l_{\underline{p}}^{c,n}\pi_{\underline{p}}^{c,n}n_{\underline{p}}^{c,r,n}+r_{\overline{p}}^{c,n}l_{\overline{p}}^{c,n}\pi_{\overline{p}}^{c,n}n_{\overline{p}}^{c,r,n})+A_c^nP_a^n, \tag{2.19c}$$

$$F_E=-\sum_{p\in p(c)}(r_{\underline{p}}^{c,n}l_{\underline{p}}^{c,n}\pi_{\underline{p}}^{c,n}\mathbf{n}_{\underline{p}}^{c,n}+r_{\overline{p}}^{c,n}l_{\overline{p}}^{c,n}\pi_{\overline{p}}^{c,n}\mathbf{n}_{\overline{p}}^{c,n})\cdot\mathbf{u}_p^n, \tag{2.19d}$$

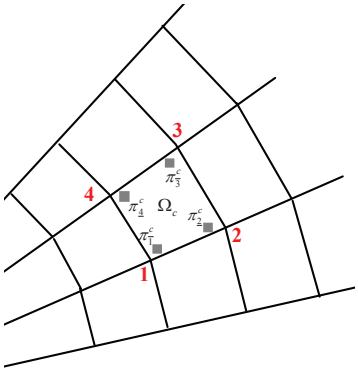

Figure 2: The definition of the pressures $\pi^c_{\underline{1}}$, $\pi^c_{\underline{2}}$, $\pi^c_{\underline{3}}$ and $\pi^c_{\underline{4}}$.

where

$$P^n_a = \frac{1}{4}(\pi^c_{\underline{1}} + \pi^c_{\underline{2}} + \pi^c_{\underline{3}} + \pi^c_{\underline{4}})$$

with $\pi^c_{\underline{1}}$, $\pi^c_{\underline{2}}$, $\pi^c_{\underline{3}}$ and $\pi^c_{\underline{4}}$ being the values of pressure related to the two radial edges of the cell Ω_c if the polar grid is used (see Fig. 2). All the variables with the superscript n represent the values of the relative variables at the n-th steps. $(n^{c,z}_{\underline{p}}, n^{c,r}_{\underline{p}})$, $(n^{c,z}_{\overline{p}}, n^{c,r}_{\overline{p}})$ are the z and r components of $\mathbf{n}^c_{\underline{p}}$, $\mathbf{n}^c_{\overline{p}}$.

The time step Δt^n is controlled by both the CFL condition and the criterion on the variation of the volume, see [20] for more details.

Remark 2.4. In general, just as shown in [20,24], all the nodal velocities can be calculated by the formulas (2.13)-(2.15) except for those located at the z coordinate line, which are obtained by imposing the boundary condition of zero normal velocity into the solver (2.13)-(2.14). However, in practice, we notice that if we use these formulas on the nodes located at the free boundary, a significant spurious heating error near this region arises. In this paper, we apply the zero-pressure boundary condition on the nodal pressures corresponding to the free boundary and the following alternative way to determine v^e_p at the free boundary, which is demonstrated to give better performance, especially for expansion problems with free boundaries:

$$v^e_p = \begin{cases} \mathbf{u}_{cl} \cdot \mathbf{n}^e_p, & cl \in \Omega, \\ \mathbf{u}_{cr} \cdot \mathbf{n}^e_p, & cr \in \Omega. \end{cases} \tag{2.20}$$

As an example, in the next subsection, we will show the comparison of the results of the free expansion problem using the above mentioned two ways to determine the nodal velocity at the free boundary.

2.2.2 Numerical tests

We have performed all the tests shown in [13] by the scheme (2.18) and obtained the expected identical results as those in [13]. In this subsection, we will give several new

tests which have not been shown in our previous papers to further verify the performance of the scheme and to validate the new implementation. Purely Lagrangian computation, the ideal gas with $\gamma=5/3$ and an initially equal-angled polar grid is used in the following tests unless otherwise stated. Reflective boundary conditions are applied to the z and r axes in all the tests. The velocity of nodes located at the z coordinate is obtained by imposing the boundary condition of zero normal velocity into the solver (2.13)-(2.14).

Test 2.1. (The free expansion problem [31]). The initial computational domain is $[0,1]\times[0,\pi/2]$ defined in the polar coordinates. The gas is initially at rest with density $\rho=1$ and pressure $P=1-(z^2+r^2)$.

This problem has the analytical solution as follows,

$$R(t)=\sqrt{1+2t^2}, \qquad u_{\tilde{\xi}}(z,r,t)=\frac{2t}{1+2t^2}\sqrt{z^2+r^2},$$
$$\rho(z,r,t)=\frac{1}{R^3}, \qquad P(z,r,t)=\frac{1}{R^5}\left(1-\frac{z^2+r^2}{R^2}\right),$$

where R is the radius of the free outer boundary and $u_{\tilde{\xi}}$ represents the value of velocity in the radial direction.

The test is performed on an initially equal-angled polar grid. Free boundary condition is applied on the outer boundary. To determine the velocity of the nodes at the free boundary, we apply the two ways mentioned in the previous subsection to calculate the normal velocity v_p^e of the cell edges that are located at the free boundary respectively. The first one is determined by the expression (2.15), the second one is determined by the expression (2.20). Fig. 3 shows the grids with 40×40 at $t=1$ obtained by the two ways to determine the nodal velocity at the free boundary. From the figures, we can see the second way gives more accurate position of the free boundary (its analytical radius should be $\sqrt{3}$ at this time). Fig. 4 gives the comparison of the internal energy at $t=1$ by using these two methods which shows that the first method produces spurious heating in the cells experiencing expansion while the second one does not.

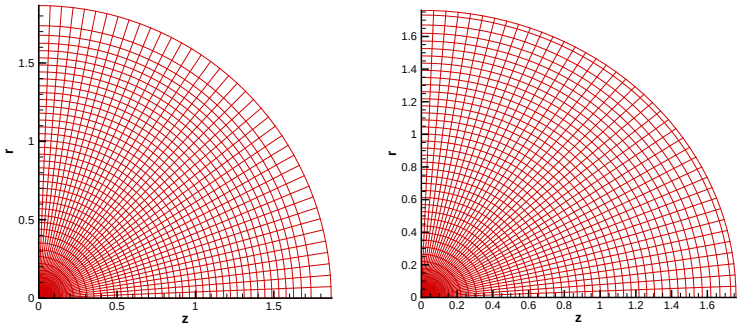

Figure 3: The grids with 40×40 cells for the free expansion problem at $t=1$. Left: the nodal velocity at the free boundary determined by the formulas (2.13)-(2.15); Right: the nodal velocity at the free boundary determined by the formulas (2.13), (2.14), (2.20).

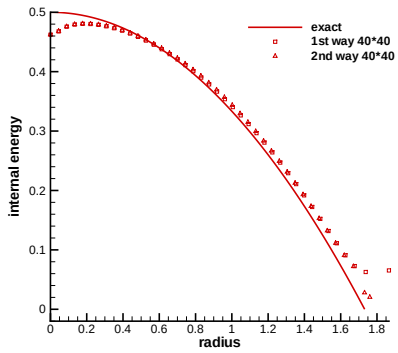

Figure 4: The comparison of the specific internal energy for the free expansion problem by using two different ways to determine the nodal velocity at the free boundary.

Test 2.2. (The Saltzman problem [15]). This is a well known difficult test case to validate the robustness of a Lagrangian scheme when the mesh is not aligned with the fluid flow. The initial mesh is 100 cells in the z-direction and 10 cells in the r-direction which is defined by

$$z(i,j)=(i-1)\Delta z+(11-j)\sin(0.01(i-1)\pi)\Delta r, \qquad r(i,j)=(j-1)\Delta r,$$

where $\Delta z=\Delta r=0.01$. The initial mesh is displayed in Fig. 5 which is deliberately distorted to set it as a more demanding test case. The left boundary of the domain is a piston which moves from left to right with a constant velocity of 1.0. The initial conditions involve a stationary gas with a unity density and an internal energy of 10^{-6}. Reflective boundary conditions are used on the right, upper and lower boundaries. Fig. 6 shows the numerical results of grid and density at the time $t=0.8$ when the shock has hit the wall at $x=1.0$ and bounced back to the left region. At this time, the shock is expected to be located at $x=0.967$, the analytical values of density are 4 and 10 in the two regions near the shock respectively. The numerical results are close to these analytical values.

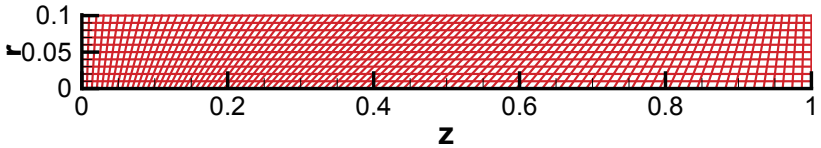

Figure 5: The initial grid of the Saltzman problem.

Test 2.3. (The one-dimensional simplified spherical ICF ignition problem). This is a simplified spherical ICF ignition problem in a cylindrical coordinate system. The model consists of two regions filled with DT gas and DT ice respectively, see the left picture in Fig. 7. The DT gas with density $0.0003\text{g}/\text{cm}^3$ is in the domain of $radius\in[0,870](\mu\text{m})$ and the DT ice with density $0.25\text{g}/\text{cm}^3$ is in the domain of $radius\in[870,950](\mu\text{m})$. A source of pressure is imposed on the outer surface of the model. Its evolution curve is shown in the

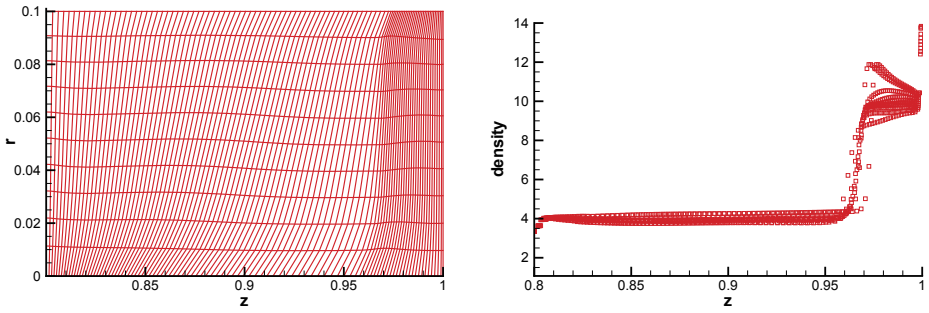

Figure 6: The results of the Saltzman problem at $t=0.8$. Left: the grid; Right: the density as a function of the z coordinate.

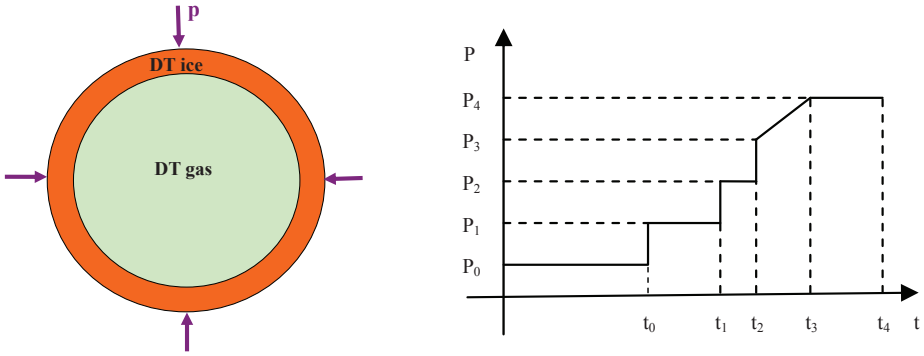

Figure 7: The simplified ICF ignition model. Left: the model; Right: the evolution curve for the source of pressure.

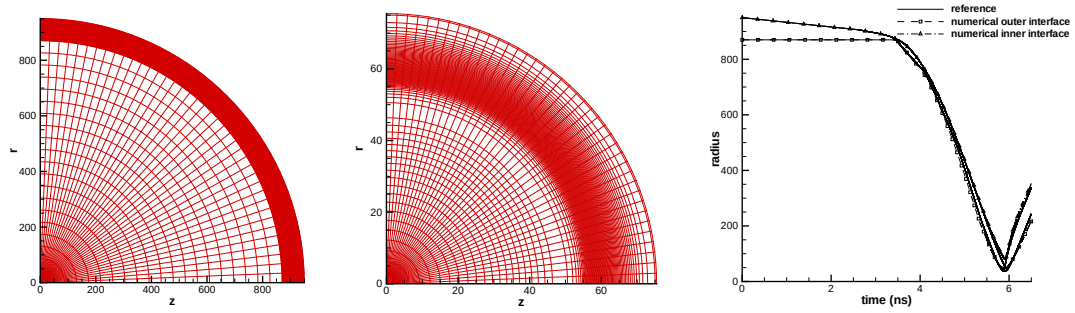

Figure 8: The results of the 1D simplified ICF ignition problem with a 90×40 grid. Left: the initial grid; Middle: the grid at $t=5.9$; Right: the trajectories of the inner and outer surfaces.

right picture in Fig. 7, where $t_0=2.613$, $t_1=3.1485$, $t_2=3.3462$, $t_3=5.0$, $t_4=6.0$(ns); $P_0=1$, $P_1=4$, $P_2=16$, $P_3=64$, $P_4=100$(Mbar). This kind of source is designed to generate four imploding shock waves coalescing near the inner surface of the fuel so that the expected high temperature and high density are obtained in the DT gas region. A 90×40 grid is applied in the 1/4-circle computational domain to test this problem. Fig. 8 shows the initial grid, the grid at the most compressed time $(t=5.9)$ and the trajectories of the inner

and outer surfaces. The reference solution is given by the one-dimensional second-order Lagrangian code in the spherical coordinate with 5000 cells. From the figures, we notice that the numerical result is symmetrical and agrees with the reference solution very well.

Test 2.4. (The two-dimensional simplified spherical ICF ignition problem). We consider further the above simplified ICF model by using a two-dimensional source of pressure. To be more specific, the following perturbation of the source of pressure given in Test 2.3 is used,

$$P=(1+\epsilon\cos k\theta)P_3,$$

where P_3 denotes the pressure source in Test 2.3, $\epsilon=0.01$ stands for the magnitude of the perturbation and $k=6$ stands for the wave number. The same initial grid as in Test 2.3 is used in this test. The results of the grid and the density at the most compressed time $(t=5.9)$ are given in Fig. 9. For this two-dimensional problem, we cannot easily obtain an analytical or reference solution. However, considering that it is difficult for most of the existing Lagrangian schemes to simulate this model to this critical time due to the serious grid distortion, the results shown in Fig. 9 demonstrate the robustness of our scheme.

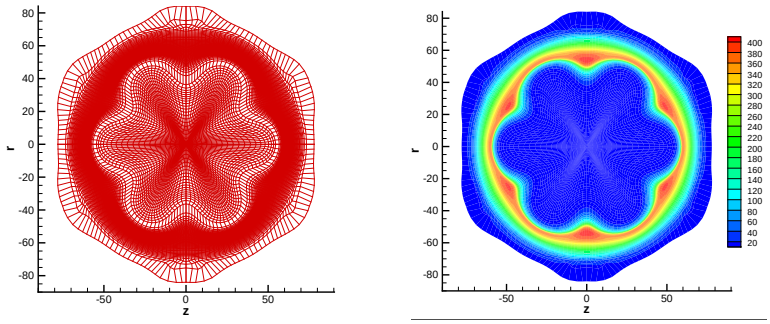

Figure 9: The results of the 2D simplified ICF ignition problem in the whole region obtained by a mirror image at $t=5.9$. Left: the grid; Right: the density contour.

3 Conservative Lagrangian scheme for the three-temperature radiation hydrodynamic equations

3.1 Three-temperature model for the ICF problem and its discretization

For the inertial confinement fusion (ICF) simulations, usually multiple internal energy equations are involved. For example, in the LARED-H code [30] which is developed to study laser target coupling and hohlraum physics, it is assumed that the electron, ion and radiation field are in local thermodynamic equilibrium (LTE) respectively, each having its own temperature, resulting in the so-called three-temperature model. In this model, the energy equation consists of three internal energy equations. To be more specific,

the three-temperature hydrodynamic equations in the cylindrical coordinates with the Lagrangian formulation have the following expression

$$\frac{d}{dt}\iint_{\Omega(t)}\rho r dz dr = 0, \tag{3.1a}$$

$$\frac{d}{dt}\iint_{\Omega(t)}\rho \mathbf{u} r dz dr = -\int_{\Gamma(t)}(P_e+P_i+P_r)\mathbf{n} ds, \tag{3.1b}$$

$$\frac{\mathrm{d}}{\mathrm{d}t}\iint_{\Omega(t)}e_e r dz dr = \iint_{\Omega(t)}(-P_e\nabla\cdot\mathbf{u}+\nabla\cdot(k_e\nabla T_e)+\rho s_e) r dz dr, \tag{3.1c}$$

$$\frac{\mathrm{d}}{\mathrm{d}t}\iint_{\Omega(t)}e_i r dz dr = \iint_{\Omega(t)}(-P_i\nabla\cdot\mathbf{u}+\nabla\cdot(k_i\nabla T_i)+\rho s_i) r dz dr, \tag{3.1d}$$

$$\frac{\mathrm{d}}{\mathrm{d}t}\iint_{\Omega(t)}e_e r dz dr = \iint_{\Omega(t)}(-P_r\nabla\cdot\mathbf{u}+\nabla\cdot(k_r\nabla T_r)+\rho s_r) r dz dr, \tag{3.1e}$$

where $\{e_e,e_i,e_r\}$, $\{P_e,P_i,P_r\}$ and $\{T_e,T_i,T_r\}$ are the internal energy, pressure and temperature of electron, ion and radiation respectively. $\{k_e,k_i,k_r\}$ are the conductivity coefficients of electron, ion and radiation respectively. $\{s_e,s_i,s_r\}$ are the source terms which have the following detailed expression,

$$\begin{pmatrix} s_e \\ s_i \\ s_r \end{pmatrix} = \begin{pmatrix} w_{ei}(T_i-T_e)+w_{er}(T_r-T_e)+s_l \\ w_{ei}(T_e-T_i) \\ w_{er}(T_e-T_r) \end{pmatrix}, \tag{3.2}$$

where w_{ei} is the electron-ion energy exchange term, w_{er} is the electron-radiation energy exchange term and s_l is the laser energy term. Besides a laser source, other sources such as that for radiation can be applied either in the energy equations or in the boundary conditions on the temperature, flux, pressure, etc.

In the LARED-H code, the laser energy term is given with a 3D ray-tracing package for computing the inverse-bremsstrahlung energy deposition rate. The 3-D laser package computes the trajectories of laser rays through the mesh. The rays are bent obeying the laws of refraction. Ray trajectories are calculated using the gradient-index geometrical optics equations. Based on the computed ray path lengths, energy is deposited in each cell by inverse bremsstrahlung, see [16] for more details. The specific definition of the terms and coefficients in Eqs. (3.1)-(3.2) which have not been discussed here can be found in [9, 32].

The electron, ion and radiation thermal conduction terms in the internal energy equations are discretized by the Kershaw's nine-point diffusion difference scheme [18]. The code uses the staggered-grid based Lagrangian hydrodynamic schemes such as those in [3, 6] to solve the mass and momentum equations and the work terms (the first right-hand-side terms) in the energy equations. The Euler forward method is used to discretize the time derivative terms in Eq. (3.1). The whole system is finally solved by an unsplit method which applies the implicit discretization to the heat conduction terms and the energy exchange terms and applies the explicit discretization to the hydrodynamics terms

and the laser energy term. The above mentioned scheme can keep the spherical symmetry property but can not keep the conservation of momentum or total energy in the cylindrical coordinates. In this paper, we would like to generalize the scheme presented in [13], with the technique described in the previous section, to the LARED-H code which can preserve both the spherical symmetry and conservation properties. In the following, we only discuss the discretization of the terms related to the hydrodynamics, as other terms are solved by the original methods used in the LARED-H code.

For the mass and momentum equations in (3.1), we use the scheme (2.18) to solve them directly. We now discuss how to discretize the work terms appearing in the internal energy equations.

Denote

$$P=P_e+P_i+P_r, \qquad W_e=-\iint_{\Omega_c} P_e\nabla\cdot\mathbf{u}rdzdr,$$
$$W_i=-\iint_{\Omega_c} P_i\nabla\cdot\mathbf{u}rdzdr, \qquad W_r=-\iint_{\Omega_c} P_r\nabla\cdot\mathbf{u}rdzdr,$$

and

$$W=W_e+W_i+W_r=-\iint_{\Omega_c} P\nabla\cdot\mathbf{u}rdzdr=-\iint_{\Omega_c}(P_e+P_i+P_r)\nabla\cdot\mathbf{u}rdzdr.$$

Then the work terms of electron and radiation W_e, W_r are discretized as follows

$$W_e\approx F_{te}:=-P_e^c\Big(\sum_{p\in p(c)}(r_{\underline{p}}^{c,n}l_{\underline{p}}^{c,n}\mathbf{n}_{\underline{p}}^{c,n}+r_{\overline{p}}^{c,n}l_{\overline{p}}^{c,n}\mathbf{n}_{\overline{p}}^{c,n})\cdot\mathbf{u}_p^n\Big), \tag{3.3a}$$

$$W_r\approx F_{tr}:=-P_r^c\Big(\sum_{p\in p(c)}(r_{\underline{p}}^{c,n}l_{\underline{p}}^{c,n}\mathbf{n}_{\underline{p}}^{c,n}+r_{\overline{p}}^{c,n}l_{\overline{p}}^{c,n}\mathbf{n}_{\overline{p}}^{c,n})\cdot\mathbf{u}_p^n\Big), \tag{3.3b}$$

where P_e^c,P_r^c are the electron and radiation pressures at the cell center which are determined by the density and corresponding internal energy in the cell Ω_c through the equation of state (EOS).

Using the technique introduced in the previous section, the work term of ion W_i is discretized in the following way,

$$\begin{aligned} W_i&=W-W_e-W_r\\ &\approx F_{ti}:=F_E-\frac{1}{2}\big[(\overline{u}_c^{z,n+1}+\overline{u}_c^{z,n})F_M^z+(\overline{u}_c^{r,n+1}+\overline{u}_c^{r,n})F_M^r\big]-F_{te}-F_{tr}, \end{aligned} \tag{3.4}$$

where F_M^z, F_M^r, F_E have the same definitions as in (2.19).

Remark 3.1. We apply the standard technique of staggered-grid based schemes such as those in [3,6] to solve the three-temperature equations. To be more specific, we discretize the electron and radiation energy equations by the central difference (3.3) and discretize the ion energy equation by (3.4) which involves (implicit) numerical viscosity through upwinding of a cell-centered scheme. This implicit numerical viscosity has an effect of converting dissipation of kinetic energy into internal energy through shock waves. This effect can further be demonstrated by the following numerical tests such as the two-material shock tube problem.

Proposition 3.1. The above described scheme for the three-temperature hydrodynamic equations (3.1) can keep the properties of spherical symmetry and the conservation for mass, momentum and total energy.

Proof. For the preservation of the conservation property, we have the following brief proof:

As the scheme (2.18) is used to discretize the mass and momentum equations in (3.1) directly, the conservation of mass and momentum is obtained automatically. For the proof of the conservation of total energy, here we only consider the hydrodynamics terms in Eq. (3.1) and assume the discretizations for the heat conduction and source terms do not destroy the conservation of total energy. Specifically, we will prove that, for the following simplified hydrodynamics equations, the scheme can keep the conservation of total energy

$$\frac{d}{dt}\iint_{\Omega(t)}\rho r dz dr = 0, \tag{3.5a}$$

$$\frac{d}{dt}\iint_{\Omega(t)}\rho \mathbf{u} r dz dr = -\int_{\Gamma(t)}(P_e+P_i+P_r)\mathbf{n} ds, \tag{3.5b}$$

$$\frac{\mathrm{d}}{\mathrm{d}t}\iint_{\Omega(t)} e_e r dz dr = \iint_{\Omega(t)} -P_e\nabla\cdot\mathbf{u} r dz dr, \tag{3.5c}$$

$$\frac{\mathrm{d}}{\mathrm{d}t}\iint_{\Omega(t)} e_i r dz dr = \iint_{\Omega(t)} -P_i\nabla\cdot\mathbf{u} r dz dr, \tag{3.5d}$$

$$\frac{\mathrm{d}}{\mathrm{d}t}\iint_{\Omega(t)} e_e r dz dr = \iint_{\Omega(t)} -P_r\nabla\cdot\mathbf{u} r dz dr. \tag{3.5e}$$

As discussed above, the momentum and energy equations in (3.5) are discretized in each cell Ω_c as follows,

$$\overline{\rho}_c^{n+1}\overline{\mathbf{u}}_c^{n+1}V_c^{n+1} - \overline{\rho}_c^{n}\overline{\mathbf{u}}_c^{n}V_c^{n} = \Delta t\mathbf{F}_M, \tag{3.6a}$$

$$\overline{e}_{e,c}^{n+1}V_c^{n+1} - \overline{e}_{e,c}^{n}V_c^{n} = \Delta t F_{te}, \tag{3.6b}$$

$$\overline{e}_{i,c}^{n+1}V_c^{n+1} - \overline{e}_{i,c}^{n}V_c^{n} = \Delta t F_{ti}, \tag{3.6c}$$

$$\overline{e}_{r,c}^{n+1}V_c^{n+1} - \overline{e}_{r,c}^{n}V_c^{n} = \Delta t F_{tr}, \tag{3.6d}$$

where $\overline{e}_{e,c}$, $\overline{e}_{i,c}$, $\overline{e}_{r,c}$ are the cell averages of electron, ion, radiation internal energy in Cell Ω_c respectively. $\mathbf{F}_M$, F_{te}, F_{ti}, F_{tr} are determined by (2.19), (3.3), (3.4) individually.

Multiplying (3.6a) by $(\overline{\mathbf{u}}_c^{n+1}+\overline{\mathbf{u}}_c^{n})/2$ and summing it with (3.6b), (3.6c), (3.6d) and using the fact that $m_c = \overline{\rho}_c^{n+1}V_c^{n+1} = \overline{\rho}_c^{n}V_c^{n}$, we then get

$$\begin{aligned}&\left[\overline{e}_{e,c}^{n+1}+\overline{e}_{i,c}^{n+1}+\overline{e}_{r,c}^{n+1}+\frac{1}{2}\overline{\rho}_c^{n+1}(\overline{\mathbf{u}}_c^{n+1})^2\right]V_c^{n+1} - \left[\overline{e}_{e,c}^{n}+\overline{e}_{i,c}^{n}+\overline{e}_{r,c}^{n}+\frac{1}{2}\overline{\rho}_c^{n}(\overline{\mathbf{u}}_c^{n})^2\right]V_c^{n}\\ =&\Delta t\left[F_{te}+F_{ti}+F_{tr}+\frac{1}{2}(\overline{\mathbf{u}}_c^{n+1}+\overline{\mathbf{u}}_c^{n})\cdot\mathbf{F}_M\right].\end{aligned}$$

Due to (3.4) and the relationship $\overline{E}_c=\overline{e}_{e,c}+\overline{e}_{i,c}+\overline{e}_{r,c}+\overline{\rho}_c\overline{\mathbf{u}}_c^2/2$, we have

$$\overline{E}_c^{n+1}V_c^{n+1}-\overline{E}_c^nV_c^n=\Delta tF_E. \tag{3.7}$$

This discretization can keep the conservation of total energy which has been shown in [13, 20]. Thus the proof of conservation is finished. □

As to the property of spherical symmetry, the steps of the proof follow the lines given in [13]. We will not repeat them here to save space.

3.2 Numerical tests for the three-temperature model

We have implemented the above approach in the LARED-H code and performed the two-material shock tube test and the ICF implosion test by using the new hydrodynamic scheme, which demonstrates the validation of our new approach. The units of time, length, mass, density and temperature are set to be ns, μm, g, g/cm^3 and K respectively unless otherwise stated.

Test 3.1. (The two-material shock tube problem). We use our two-dimensional code to test a one-dimensional two-material shock tube problem similar to that given in [2]. The computational domain is $[0,1]\times[0,0.1]$(cm) whose left region consists of Aluminum (Al) and right region is filled with plastic (CH). The initial interface is located at $z=0.5$cm. The initial condition is as follows

$$(\rho,T_e,T_i,T_r,u_z,u_r)^T=\begin{cases}(2.7,2.32\times10^8,2.32\times10^8,2.32\times10^6,0,0)^T, & 0\le z\le 0.5,\\ (1,1.16\times10^8,1.16\times10^8,1.16\times10^6,0,0)^T, & 0.5\le z\le 1.\end{cases} \tag{3.8}$$

The ideal gas equation of state is used to both materials Al and CH. The final time is $t=2$. We perform the purely Lagrangian simulation in two cases. The reference solutions for both cases are produced by the simulation with 2000×4 cells. Firstly, we test the problem by the three-temperature model, that is, simulating Eq. (3.1)-(3.2) in a normal way. Fig. 10 shows the results of density, electron temperature and radiation temperature at the section $r=0.05$cm with 100×4, 200×4, 400×4 cells respectively. The result of the ion temperature is similar to that of the electron temperature. In this case, we observe that most energy of electron and ion is converted to the radiation energy and the radiation is close to a constant state but the electron and ion are not. The numerical results of all the variables converge to the reference solutions asymptotically. Secondly, we test the problem by setting the electron-radiation energy exchange term w_{er} in Eq. (3.2) to be zero. This treatment on w_{er} results in the test simulated by a two-temperature (electron and ion) model which is similar to that used in [2]. Fig. 11 shows the results of density and electron temperature at the section $r=0.05$cm with three different refined grids. The figures reflect the convergence trend of the numerical solutions toward the reference solutions and no oscillation is observed near the interface. These results are comparable to those shown in [2].

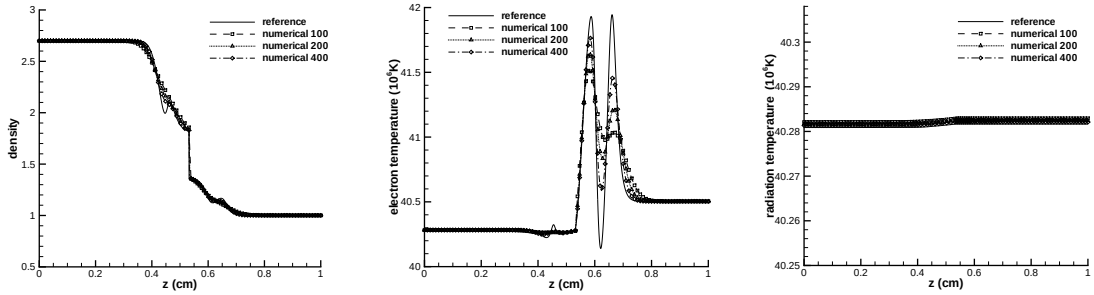

Figure 10: The results of the two-material shock tube problem by simulating the three-temperature equations (3.1)-(3.2) at $t=2$. Left: density; Middle: electron temperature; Right: radiation temperature.

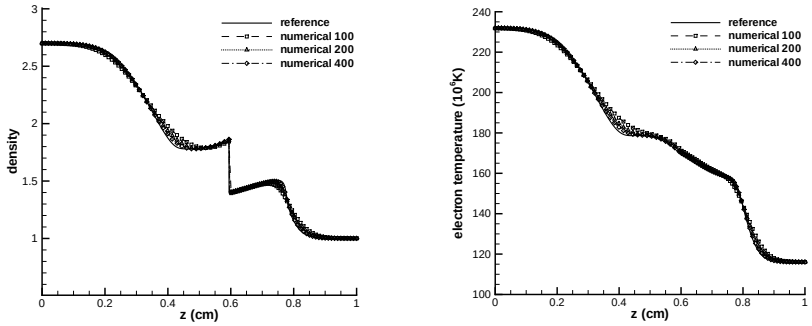

Figure 11: The results of the two-material shock tube problem by simulating the three-temperature equations (3.1)-(3.2) with $w_{er}=0$ at $t=2$. Left: density; Right: electron temperature.

Test 3.2. (The ICF implosion test). A capsule is a spherical shell filled with low-density gas. The shell with carbon-hydrogen polymer (CH) is composed of an outer region $r\in[100,112]$, which forms the ablator and an inner region $r\in[0,100]$ of deuterium-tritium (DT), which forms the main fuel. A radiation source temperature is imposed on the outer surface of the capsule which changes with time as the curve shown in Fig. 12. At the initial time, the whole region is at rest. The density of the DT material is 0.0038 and the density of the CH material is 1. The electron, ion and radiation have the same

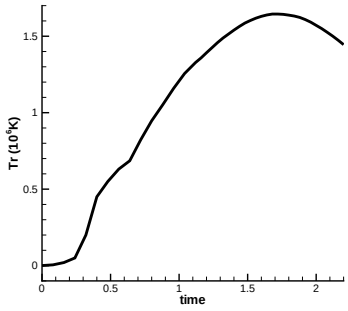

Figure 12: The evolution curve of the source radiation temperature.

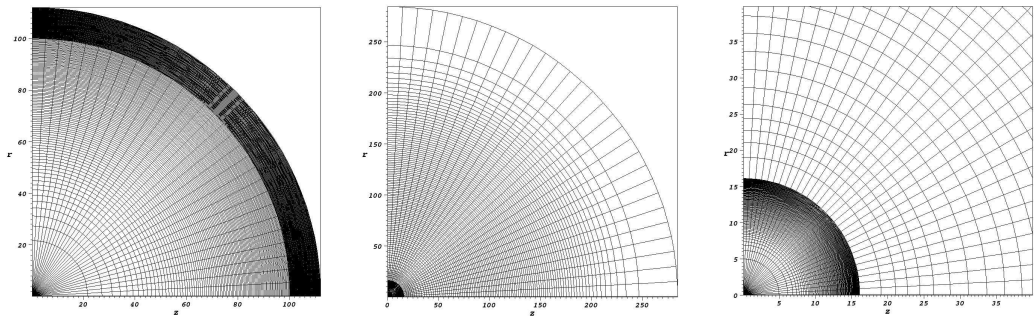

Figure 13: The results of the ICF implosion problem with a 100×30 grid. Left: the initial grid; Middle: the grid at the most compressed time $(t=1.54)$; Right: the zoomed grid near the center at $t=1.54ns$.

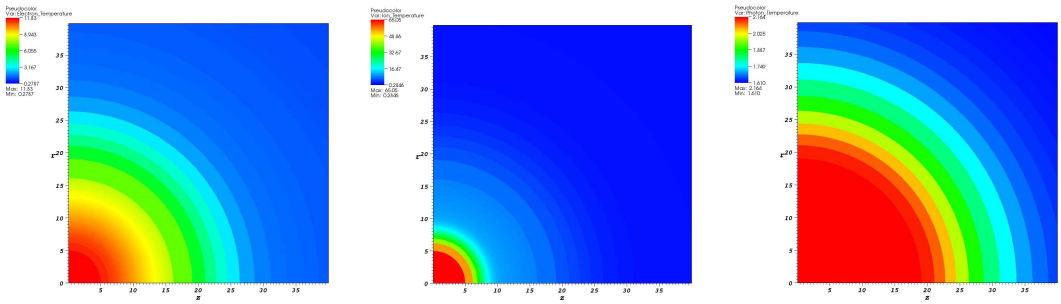

Figure 14: The results of the ICF implosion problem with a 100×30 grid at the most compressed time $(t=1.54)$. Left: electron temperature; Middle: ion temperature; Right: radiation temperature (the temperature unit is 10^6K).

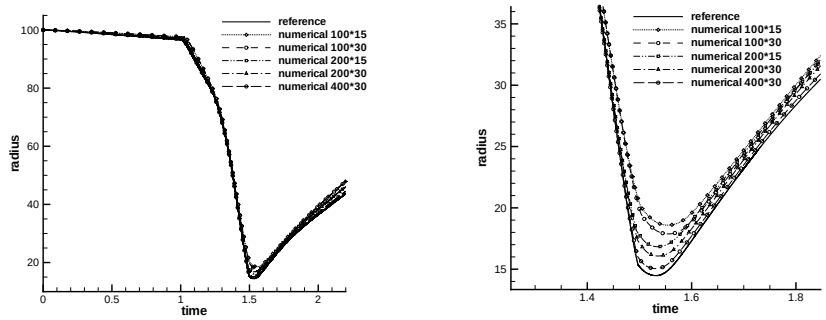

Figure 15: The trajectories of the interface by using different grids. Left: the whole time region; Right: the zoomed-in time region near the most compressed time. Solid line: the reference solution; dashed line: the computational solution.

temperature as 300°. We simulate this model with the Lagrangian scheme (2.18), (3.3)-(3.4) on a sequence of progressively refined grids with 100×15, 100×30, 200×15, 200×30, 400×15 cells. The final time is $t=2.2$. The numerical result with a 800×30 grid is taken as the reference solution. Figs. 13 and 14 show the results with a 100×30 grid at the most compressed time $(t=1.54)$. We notice the expected symmetrical results both in the grid

and in the temperature. Fig. 15 shows the trajectories of the interface simulated by the above mentioned different grids respectively. Comparing with the reference solution, we can observe the asymptotically convergent trend of the numerical solutions which demonstrates the validation of our hydrodynamic discretization strategy for the three-temperature equations.

4 Concluding remarks

Many multi-material hydrodynamic application problems involve multiple internal energy equations such as those for electron, ion and radiation and their simulation codes are usually based on staggered-grid Lagrangian schemes which solve the internal energy equations directly. This paper introduces a strategy to apply cell-centered Lagrangian schemes, which usually are based on the Euler equations in the total energy form, to solve the compressible fluid flow with multiple internal energy equations without loss of its original good properties.

We have established an equivalency relationship between the cell-centered discretizations of the Euler equations in the forms of the total energy and of the internal energy. Through a modification on the implementation, without loss of any of its good properties, the cell-centered Lagrangian scheme can be used to solve one or multiple internal energy equations directly. As a numerical test, the strategy of solving the three-temperature equations by the cell-centered Lagrangian scheme is proposed and implemented in the LARED-H radiation hydrodynamic code. This application does not require any modification to the original structure of the code. Several two dimensional numerical examples for both Euler equations and three-temperature hydrodynamic equations in two-dimensional cylindrical coordinates are presented to demonstrate the validation of the schemes in terms of conservation, symmetry, accuracy, non-oscillation and robustness. In future work, we will investigate a second order accurate extension of the cell-centered Lagrangian scheme with the properties of spherical symmetry and conservation, which is suitable for the Euler equations both in the forms of the total energy and of the internal energy.

Acknowledgments

J. Cheng is supported in part by NSFC grants 10972043, 10931004 and 91130002. Additional support is provided by the National Basic Research Program of China under grant 2011CB309702. C.-W. Shu is supported in part by ARO grant W911NF-08-1-0520 and NSF grant DMS-0809086. Q. Zeng is supported in part by NSFC grant 11001026 and CAEP project 2011B0202041. The authors also thank Professor Jinghong Li for his help in providing the exact solution for the free expansion problem in Section 2.2.2.

References

[1] D. J. Benson, Momentum advection on a staggered mesh, J. Comput. Phys., 100 (1992), 143–162.

[2] J. Breil, S. Galera and P.-H. Maire, Multi-material ALE computation in inertial confinement fusion code CHIC, Comput. Fluids, 46 (2011), 161–167.

[3] P. L. Browne, Integrated gradients: a derivation of some difference forms for the equation of motion for compressible flow in two-dimensional Lagrangian hydrodynamics, using integration of pressures over surfaces, Los Alamos National Laboratory Report LA-2105872-MS, 1986.

[4] A. Burbeau-Augoula, A node-centered artificial viscosity method for two-dimensional Lagrangian hydrodynamics calculations on a staggered grid, Commun. Comput. Phys., 8 (2010), 877–900.

[5] J. C. Campbell and M. J. Shashkov, A tensor artificial viscosity using a mimetic finite difference algorithm, J. Comput. Phys., 172 (2001), 739–765.

[6] E. J. Caramana, D. E. Burton, M. J. Shashkov and P. P. Whalen, The construction of compatible hydrodynamics algorithms utilizing conservation of total energy, J. Comput. Phys., 146 (1998), 227–262.

[7] E. J. Caramana, M. J. Shashkov and P. P. Whalen, Formulations of artificial viscosity for multidimensional shock wave computations, J. Comput. Phys., 144 (1998), 70–97.

[8] G. Carré, S. Delpino, B. Després and E. Labourasse, A cell-centered Lagrangian hydrodynamics scheme in arbitrary dimension, J. Comput. Phys., 228 (2009), 5160–5183.

[9] T. Chang, G. Chen and L. Shen, A numerical method for solving the stiff problem in modeling laser target coupling, Comput. Math. Math. Phys., 33 (1993), 805–814.

[10] J. Cheng and C.-W. Shu, A high order ENO conservative Lagrangian type scheme for the compressible Euler equations, J. Comput. Phys., 227 (2007), 1567–1596.

[11] J. Cheng and C.-W. Shu, A third order conservative Lagrangian type scheme on curvilinear meshes for the compressible Euler equation, Commun. Comput. Phys., 4 (2008), 1008–1024.

[12] J. Cheng and C.-W. Shu, A cell-centered Lagrangian scheme with the preservation of symmetry and conservation properties for compressible fluid flows in two-dimensional cylindrical geometry, J. Comput. Phys., 229 (2010), 7191–7206.

[13] J. Cheng and C.-W. Shu, Improvement on spherical symmetry in two-dimensional cylindrical coordinates for a class of control volume Lagrangian schemes, Commun. Comput. Phys., 11 (2012), 1144–1168.

[14] B. Després and C. Mazeran, Lagrangian gas dynamics in two dimensions and Lagrangian systems, Arch. Rational Mech. Anal., 178 (2005), 327–372.

[15] J. K. Dukowicz and B. J. A. Meltz, Vorticity errors in multidimensional Lagrangian codes, J. Comput. Phys., 99 (1992), 115–134.

[16] A. Friedman, Three-dimensional laser ray tracing on a *r*-*z* Lagrangian mesh, Laser Programs Annual Report, UCRL-50021-83 (1983), 3–51.

[17] J. A. Harte, W. E. Alley, D. S. Bailey, J. L. Eddleman and G. B. Zimmerman, LASNEX-a 2-D physics code for modeling ICF, Lawrence Livermore National Laboratory Report UCRL-LR-105821-96-4 (1996), 150–164.

[18] D. S. Kershaw, Differencing of the diffusion equation in Lagrangian hydrodynamic codes, J. Comput. Phys., 39 (1981), 375–395.

[19] W. Liu, J. Cheng and C.-W. Shu, High order conservative Lagrangian schemes With Lax-Wendroff type time discretization for the compressible Euler equations, J. Comput. Phys.,

228 (2009), 8872–8891.
[20] P.-H. Maire, A high-order cell-centered Lagrangian scheme for compressible fluid flows in two-dimensional cylindrical geometry, J. Comput. Phys., 228 (2009), 6882–6915.
[21] P.-H. Maire, A high-order cell-centered Lagrangian scheme for two-dimensional compressible fluid flows on unstructured meshes, J. Comput. Phys., 228 (2009), 2391–2425.
[22] P.-H. Maire, A high-order one-step sub-cell force-based discretization for cell-centered Lagrangian hydrodynamics on polygonal grids, Comput. Fluids, 46 (2011), 341–347.
[23] P.-H. Maire, A unified sub-cell force-based discretization for cell-centered Lagrangian hydrodynamics on polygonal grids, Int. J. Numer. Methods Fluids, 65 (2011), 1281–1294.
[24] P.-H. Maire, R. Abgrall, J. Breil and J. Ovadia, A cell-centered Lagrangian scheme for compressible flow problems, SIAM J. Sci. Comput., 29 (2007), 1781–1824.
[25] P.-H. Maire, R. Loubère and P. Vachal, Staggered Lagrangian discretization based on cell-centered Riemann solver and associated hydrodynamics scheme, Commun. Comput. Phys., 10 (2011), 940–978.
[26] P.-H. Maire and B. Nkonga, Multi-scale Godunov-type method for cell-centered discrete Lagrangian hydrodynamics, J. Comput. Phys., 228 (2009), 799–821.
[27] M. M. Marinak, S. W. Haan and R. E. Tipton, Three-dimensional simulations of national ignition facility capsule implosions with HYDRA, Lawrence Livermore National Laboratory Report UCRL-LR-105821-96-4 (1996), 143–149.
[28] C. D. Munz, On Godunov-type schemes for Lagrangian gas dynamics, SIAM J. Numer. Anal., 31 (1994), 17–42.
[29] J. von Neumann and R. D. Richtmyer, A method for the calculation of hydrodynamics shocks, J. Appl. Phys., 21 (1950), 232–237.
[30] W. B. Pei, The construction of simulation algorithms for laser fusion, Commun. Comput. Phys., 2 (2007), 255–270.
[31] L. I. Sedov, Similarity and Dimensional Methods in Mechanics, Academic Press, New York, 1959.
[32] G. Wang and T. Chang, Laser *X*-ray conversion and electron thermal conductivity, Plasma Sci. Tech., 3 (2001), 653–658.